Magnetic Taylor-Proudman Constraint Explains Flows into the Tangent Cylinder

Alban Pothérat* and Kélig Aujogue Coventry University, Centre for Fluid and Complex Systems, Mile Lane, Coventry CV1 2NL, UK

François Debray

Laboratoire National des Champs Magnétiques Intenses (LNCMI), CNRS UPR 3228, EMFL, Université Toulouse III - Paul Sabatier, Université Fédérale Toulouse Midi-Pyrénées, Institut National des Sciences Appliquées, Université Grenoble Alpes, 38042 Grenoble CEDEX, France (Dated: September 13, 2024)

Tangent Cylinders (TCs) have shaped our understanding of planetary dynamos and liquid cores. The Taylor-Proudman Constraint (TPC) due to planetary rotation creates these imaginary surfaces separating polar and equatorial regions but cannot explain the flows meandering through them. Here we establish and verify experimentally that magnetic fields aligned with rotation drive flows into TCs, linked to the flows along TCs by a magnetic Taylor-Proudman constraint. This constraint explains and quantifies how magnetic fields reshape rotating flows in planetary interiors and magnetorotating flows in general.

Geophysical and astrophysical flows, whether atmospheres, accretion disks, stellar or planetary interiors are often strongly constrained by the Coriolis force produced by background rotation. The Taylor-Proudman Constraint (TPC) expresses that rotation mainly renders the flow 2D, and 2D-solenoidal in the plane normal to rotation [1–3]. To remain 2D and 2D-solenoidal in planetary interiors shaped as spherical shells, the flow must follow geostrophic contours, aligned with surfaces of constant height, i.e. concentric cylinders [3]. For this reason, in planetary interiors with a solid inner core, the "tangent cylinder" (TC, Fig. 1) extruded from the solid core along the rotation axis, is often considered as a mechanical barrier separating polar and equatorial regions. Both regions are convective, but with different dynamics and they are believed to play different roles in the dynamo mechanism that sustains planetary magnetic fields [4–8].

The paradox, here is that many dynamo theories, especially for the Earth, demand that the Lorentz and the Coriolis forces be of the same order, i.e. in the magnetostrophic regime, to recover large-scale magnetic fields [9, 10]. Within the TC too, the TPC determines the dynamics of convective Taylor columns [11–13], and the Lorentz force needs to act at the leading order to recover the large structures conducive to dynamo action there [10, 14–19]. However, where the Lorentz forces competes with the Coriolis force, the TPC is violated [20– 23]. The scenario of a flow structure articulated around an impermeable TC then breaks down as it cannot explain recently discovered flows meandering in and out of it [7, 24]. Interestingly, magnetohydrodynamic (MHD) flows in a homogeneous magnetic field exhibit similar tendencies to two-dimensionality to rotating flows [25–28]. and also follow geostrophiclike contours aligned with socalled "characteristic surfaces" [29–31]. Yet, although

both axial magnetic fields and rotation act individually alike, a theory for their combined action is both missing and needed to understand the flow in the TC region, and how Lorentz and Coriolis forces constrain the convective structures inside it. Here we derive and experimentally verify the physical foundation of such a theory.

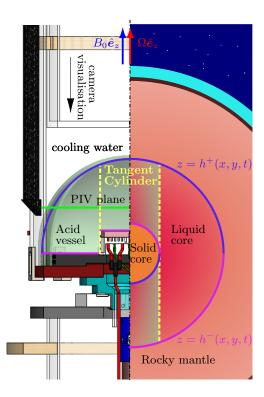


FIG. 1. Sketch of the Earth's structure with liquid outer core and solid inner core (right) and the Little Earth Experiment, its rotating hemisphere filled with sulphuric acid, protruding heater, cooling tank and height-adjustable PIV system (left).

^{*} alban.potherat@coventry.ac.uk

 ν , electric conductivity σ) with boundaries at $z=h^-(x,y,t)$ and $z=h^+(x,y,t)$, subject to a magnetic field $\boldsymbol{B}(x,y,z,t)$, assumed along \hat{e}_z for simplicity, and to a constant background rotation $\Omega \hat{e}_z$. Splitting vectors and operators into their components along and normal to \hat{e}_z (subscripts z and $_\perp$), e.g. $\nabla_\perp = (\partial_x, \partial_y)$, the dimensionless velocity \boldsymbol{u} , pressure p and electric current \boldsymbol{J} are governed by the Navier-Stokes equations

$$Ro(\partial_t + \boldsymbol{u} \cdot \nabla) \boldsymbol{u}_{\perp} + \nabla_{\perp} p = (\boldsymbol{u}_{\perp} + \Lambda \boldsymbol{J}_{\perp} B_z) \times \hat{\boldsymbol{e}}_z + Ek\Delta \boldsymbol{u}_{\perp}$$

$$Ro(\partial_t + \mathbf{u} \cdot \nabla)u_z + \partial_z p = f_b + Ek\Delta u_z, \tag{2}$$

$$\nabla \cdot \boldsymbol{u} = 0. \tag{3}$$

The Ekman, Rossby numbers $Ek = \nu/(2\Omega h_0^2)$, $Ro = U/(2\Omega h_0)$, and buoyancy force $f_b = \mathcal{O}(Ro)[32]$ based on typical velocity U and outer core shell thickness h_0 are very small in the regime of fast rotation relevant to planets (for the Earth $Ek \simeq 10^{-15}$ and $Ro \gtrsim 10^{-6}$), but the Elsasser number $\Lambda = \sigma B_0^2/(2\rho\Omega) \in [10^{-1}, 10^2]$ based on typical axial field B_0 is not [33]. The electric current J is expressed by Ohm's law in terms of the electric potential ϕ and magnetic vector-potential A, and satisfies charge conservation,

$$\mathbf{J} = -\nabla \phi + B_z \mathbf{u} \times \hat{\mathbf{e}}_z + \partial_t \mathbf{A}, \qquad \nabla \cdot \mathbf{J} = 0.$$
 (4)

In geophysical context, these equations are usually closed with the induction equation and magnetic flux conservation. The magnetic TPC, however, only requires an expression of the electric current. The idea is to express the total Lorentz-Coriolis force as the product of a single solenoidal current \mathbf{c} and $\hat{\mathbf{e}}_z$. \mathbf{c} is chosen as the compound current of mass and charge $\mathbf{c}_\perp = \mathbf{u}_\perp + \Lambda B_z \mathbf{J}_\perp$ and its vertical component $c_z = u_z + \Lambda(B_z J_z - \int \mathbf{J} \cdot \nabla B_z dz)$ is defined up to an integration constant to ensure conservation of the compound massic and electric charge associated to \mathbf{c} , i.e. $\nabla \cdot \mathbf{c} = 0$. Then at $\mathcal{O}(Ek, Ro)$, Eqs. (1), (2) imply that bulk variables (denoted $\tilde{}$) satisfy the "magnetic Taylor-Proudman constraint" (MTPC) [22, 23],

$$\partial_z \widetilde{\boldsymbol{c}}_{\perp} = \partial_z \widetilde{\boldsymbol{u}}_{\perp} + \Lambda \partial_z (B_z \widetilde{\boldsymbol{J}}_{\perp}) = 0,$$
 (5)

$$\nabla_{\perp} \cdot \widetilde{\boldsymbol{c}}_{\perp} = \nabla_{\perp} \cdot \widetilde{\boldsymbol{u}}_{\perp} + \Lambda \nabla_{\perp} \cdot (B_z \widetilde{\boldsymbol{J}}_{\perp}) = 0. \tag{6}$$

These equations express that in the rapidly rotating limit, the *current* becomes quasi-2D and quasihorizontally solenoidal. Without magnetic field, the bulk horizontal velocity $\tilde{\boldsymbol{u}}_{\perp}$ becomes 2D and horizontally solenoidal. Here, by contrast, $\tilde{\boldsymbol{u}}_{\perp}$ may be z-dependent and horizontally divergent, as long as $\Lambda \tilde{\boldsymbol{J}}_{\perp} B_z$ possesses the opposite z-dependence and horizontal divergence.

The magnetic counterpart of the topological constraint forcing the flow along geostrophic contours is found by integrating the conservation of compound charge $(\nabla \cdot \mathbf{c} = 0)$ along \hat{e}_z . Noting that regardless of the boundary conditions at $z = h^{\pm}$, the current at each boundary $c_z(z = h^{\pm})$ is the sum of the current due to the motion of the boundaries (neglecting the electric displacement current) and the current through them c_m^{\pm} ,

$$c_z(z = h^{\pm}) = \partial_t h^{\pm} + c_{\perp}^{\pm} \cdot \nabla_{\perp} h^{\pm} + c_w^{\pm},$$
 (7)

it follows that

$$\int_{h^{-}}^{h^{+}} \nabla_{\perp} \cdot \boldsymbol{c}_{\perp} dz = c_{w} - \partial_{t} h - \boldsymbol{c}_{\perp}^{+} \cdot \nabla_{\perp} h^{+} + \boldsymbol{c}_{\perp}^{-} \cdot \nabla_{\perp} h^{-},$$
(8)

where $h = h^+ - h^-$ and $c_w = c_w^- - c_w^+$. To account for the viscous boundary layers of thickness $\delta \sim Ek^{1/2}$ [34] at $z = h^{\pm}$, we decompose the current \boldsymbol{c} into its bulk value $\tilde{\boldsymbol{c}}$ satisfying Eqs. (5), (6) and two corrections for the boundary layers $\boldsymbol{c}^{\text{BL}^{\pm}} - \tilde{\boldsymbol{c}}$, which vanish in the bulk,

$$\lim_{|z-h^{\pm}|\delta^{-1}\to\infty} c^{\mathrm{BL}^{\pm}} - \widetilde{c} = 0.$$
 (9)

Then, using the Leibniz integral rule,

$$\int_{h^{-}}^{h^{+}} \nabla_{\perp} \cdot \boldsymbol{c}_{\perp} dz = \widetilde{\boldsymbol{c}}_{\perp} \cdot \nabla_{\perp} \int_{h^{-}}^{h^{+}} dz \qquad (10)$$

$$+ (\nabla_{\perp} \cdot \widetilde{\boldsymbol{c}}_{\perp}) \int_{h^{-}}^{h^{+}} dz - \boldsymbol{c}_{\perp}^{+} \cdot \nabla_{\perp} h^{+} + \boldsymbol{c}_{\perp}^{-} \cdot \nabla_{\perp} h^{-}$$

$$+ \nabla_{\perp} \cdot \int_{h^{-}}^{h^{+}} \boldsymbol{c}_{\perp}^{\mathrm{BL}^{-}} - \widetilde{\boldsymbol{c}}_{\perp} dz + \nabla_{\perp} \cdot \int_{h^{-}}^{h^{+}} \boldsymbol{c}_{\perp}^{\mathrm{BL}^{+}} - \widetilde{\boldsymbol{c}}_{\perp} dz.$$

The second term in the rhs is $\mathcal{O}(Ek, Ro)$ due to the MTPC (6). The last two terms stem from the current generated within the boundary layers to balance viscous forces, and fed into the bulk. From the compound charge conservation in the boundary layer, these scale as $c_{\perp}\delta = \mathcal{O}(Ek^{1/2})$. Then from (8) and (10), the bulk current obeys the "topological MTPC":

$$\widetilde{\boldsymbol{c}}_{\perp} \cdot \nabla_{\perp} h = c_0 + \mathcal{O}(Ek^{1/2}, Ro), \tag{11}$$

where $c_0 = -\partial_t h + c_w$. Equation (11) generalizes the concept of geostrophic contour to include not only the effect of the Lorentz force but also permeable, electrically conducting and moving boundaries: when boundaries are impermeable to \boldsymbol{c} ($c_w = 0$) and steady ($\partial_t h = 0$), it constrains the quasi-2D current $\tilde{\boldsymbol{c}}_\perp$ to follow the geostrophic contours. The current may however deflect from them to absorb current (c_0) either incurred by the motion of the boundaries ($-\partial_t h$) or fed through them (c_w) if they are not impermeable or not electrically insulating.

We can now express the MTPC in terms of the velocity field: Eq. (11) expresses the geometric constraint on a quasi-2D solenoidal current in a 3D domain, regardless of the definition of that current, so that Eq. (11) and Ohm's law (4) impose independent constraints from which J can be eliminated. Denoting normal and tangential components to a given geostrophic contour in the z-averaged plane by indices n and s, and $u_0 = c_0(\partial_n h)^{-1}$, these imply (dropping tildes)

$$u_n + \Lambda B_z J_n = u_0 + \mathcal{O}(Ek^{1/2}, Ro), \tag{12}$$

$$J_n = -\nabla_n \phi + B_z u_s + \partial_t A_n. \tag{13}$$

Using electric charge conservation and Ohm's law (4), and considering time-averaged quantities (denoted $\langle \cdot \rangle_t$),

(12) and (13) yield the "kinematic MTPC",

$$\Delta \langle B_z^{-1}(u_n - u_0) \rangle_t + \Lambda [\nabla (\nabla \cdot \langle B_z u_n \rangle_t \hat{\boldsymbol{e}}_s) \cdot \hat{\boldsymbol{e}}_n + \Delta_{zs} \langle B_z u_s \rangle_t] = 0. (14)$$

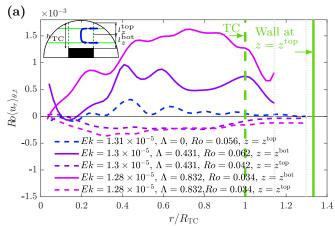
The key result here is that unlike the current c_{\perp} , the flow u_{\perp} does not follow the geostrophic contours, even if $c_0 = 0$. Instead, it is constrained by Eq. (14) to cross them. In planetary interiors with a solid core, flows across TCs have been observed or simulated but never quantified [20, 23, 24]. The kinetic MTPC (14) can measure which part of these through-flows is incurred by the axial component of the planetary magnetic field.

We shall now seek experimental evidence for these flows and for their compliance to the MTPC in a simple TC geometry. Experiments are performed in the "Little Earth Experiment" (LEE) device [35-37]. LEE is a model for the convection in the TC subject to background rotation and externally imposed axial magnetic field $B = B_0 \hat{e}_z$. The working fluid is sulphuric acid at 30% mass (viscosity $\nu = 1.3 \times 10^6 \text{ m}^2/\text{s}$, density $\rho = 1.3$ kg/m³, thermal expansion coefficient $\alpha = 5.5 \times 10^{-4} \text{ K}^{-1}$, thermal diffusivity $\kappa = 1.7 \times 10^{-7} \text{ m}^2/\text{s}$ and Prandtl number Pr = 12). Its transparency and electric conductivity $(\sigma = 83 \pm 2 \text{ Sm})$ make it the ideal choice for optical velocimetry in MHD flows [38, 39]. MHD experiments are usually conducted with liquid metals, with an electrical conductivity $\sim 10^4$ higher than sulfuric acid. Hence, to keep $\Lambda = \sigma B_0^2/(2\rho\Omega) \sim 1$ with $Ek \sim 10^{-5}$, magnetic fields ~ 10 T are needed, i.e. $\sim 10^2$ times greater than in liquid metal convection experiments [40, 41].

At LEE's heart lies a hemispherical transparent vessel filled with the acid (inner diameter 2R = 0.285 m), rotating around its vertical axis (Fig. 1). It is placed at the bottom of a cylindrical tank filled with water that ensures a constant, cold temperature T_C at all its boundaries but the bottom one. At the bottom, a coaxial cylindrical heating element (radius $R_{\rm TC} = 0.05$ m) protruding by $h_H = 0.0225$ m into the vessel fulfils two functions: first, its upper surface is kept at fixed hot temperature T_H to create an unstable temperature gradient prone to drive convection within the vessel. Second, its edge incurs a radial jump in domain height akin to the equatorial edge of the Earth's inner core, where a TC develops under fast rotation. The heater thus acts as a solid core and the hemispherical vessel wall represents the core-mantle boundary. The heater side wall and the vessel bottom wall are thermally insulated.

In acid, the magnetic diffusivity η is much greater than in metals, so for typical velocities of 10^{-3} to 10^{-1} ms⁻¹, the magnetic Reynolds number $Rm = Uh_0/\eta = U(R-h_H)/\eta$ measuring the ratio of magnetic field advection to magnetic diffusion is, at most around 10^{-6} . This places LEE in the quasistatic MHD (QSMHD) regime for which the induced magnetic field is negligible compared to the externally imposed magnetic field B_0 , so $B_z = 1$ [42].

Particle Image Velocimetry (PIV) provides two timedependent velocity components in two planes: at z^{bot} = $0.22h_0 = 0.24h_{\rm TC}$, above the heater and $z^{\rm top} = 0.74h_0 = 0.8h_{\rm TC}$, just below the point where the TC meets the inner vessel wall ($h_{\rm TC}$ is the TC's height at $r=R_{\rm TC}$). The temperature is measured at the heater surface and at the outer surface of the acid vessel wall with thermocouples, and time-averaged to calculate the free-fall velocity $U = [g\alpha(T_H - T_C)h_0]^{1/2}$ and Ro[32]. Velocity fields are then recorded over 10 min when the difference between these temperatures is statistically steady. All data presented here is averaged over that time.



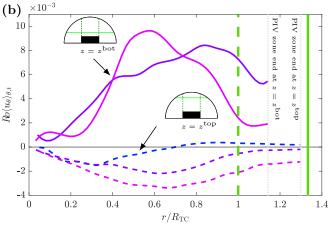


FIG. 2. Time and azimuthally averaged radial profiles of radial (a) and azimuthal (b) velocities in LEE, renormalized by rotation speed, which is more precisely measured in LEE than U. The inset sketches show (a) the single cell recirculation and (a), (b) the positions of the PIV planes.

The TC in LEE provides a geostrophic contour to test the relation predicted by the MTPC between the time-averaged azimuthal flow along it and radial flow through it without boundary current $(c_0 = 0)$ [indices (s,n) become (θ,r) in Eq. (14)]. While in the absence of magnetic field, the classical TPC extinguishes the flow through the TC when $Ek \ll 1$ and $Ro \ll 1$ [36, 43], the MTPC predicts that any azimuthal flow with a nonlinear z-dependence should incur a radial flow for $\Lambda > 0$. This flow is tracked through the azimuthally and time-averaged profiles of both velocity components

in both PIV planes. The examples plotted in Fig. 2 for $Ro \in [0.034, 0.062]$, $Ek \simeq 1.3 \times 10^{-5}$ and Λ from 0 to 0.832, span the geostrophic and magnetostrophic regimes where the MTPC applies. Magnetic $(\Lambda > 0)$ and nonmagnetic ($\Lambda = 0$) cases exhibit very different velocity profiles: while a significant azimuthal flow exists in all cases (in the nonmagnetic case, it is due to the thermal wind incurred by the radial temperature gradient [36]); the nonmagnetic flow only has a nonzero radial component in localized convective plumes within the TC $(r/R_{\rm TC} < 1)$, visible through radial oscillations in the profile. The radial velocity also remains 0 to within measurement precision at the TC boundary. The thermal plumes and corresponding oscillations subsist for $\Lambda > 0$ in the top plane. In stark contrast to the nonmagnetic case, however, a radially converging inflow occupies the entire TC in the top plane. In the bottom plane, a radial flow also appears for $\Lambda > 0$ but outward. Hence, the patterns of radial velocity on both planes imply that a meridional recirculation made of at least one cell crosses the TC boundary when $\Lambda > 0$. Furthermore, the intensity of this recirculation relative to the azimuthal flow increases with Λ , and is accompanied by a much stronger zonal flow than for $\Lambda = 0$. This flow structure subsists at all background rotations ($Ek \in \{0.82, 1.3, 3\} \times 10^{-5}$) and forcing parameters $(5 \times 10^{-4} \le Ro \le 0.3)$ we explored, regardless of variations in flow topology. Both the meridional flow pattern and the enhanced zonal flow are consistent with the relation between radial and azimuthal flow predicted by the MTPC (14). We shall now quantify this relation across LEE's parameter range.

LEE's 2D PIV data cannot give the derivatives of the velocity in both axial and radial directions that a local evaluation of the MTPC terms would demand. Hence the MTPC is averaged azimuthally, and radially within the TC to yield a scaling relation more amenable to experimental comparison (see Supplementary Material [44]):

$$\langle ru_r(z)\rangle_{t,\theta,r\leq R_{\rm TC}} \sim K(z)[\Lambda\langle ru_\theta\rangle_{t,\theta,r\leq R_{\rm TC}}]_{z^{\rm bot}}^{z^{\rm top}}.$$
 (15)

Coefficient K(z) is obtained in each PIV measurement plane at $z=z^{\rm bot}$ and $z=z^{\rm top}$ from measurements in both planes, by estimating derivatives in Eq. (14) as the ratio of velocities averaged over horizontal sections of the TC to the length scales of velocity gradients: the length scale for $\partial_{zz}^2 u_{\theta}$ between the two PIV planes is the distance between them. For $\partial_{zz}^2 u_r$, the length scales near the top and bottom planes may differ and are constrained by mass conservation, assuming a single meridional recirculation cell.

Both sides of Eq. (15) are shown in Fig. 3(a). The data collapses approximately along $\langle ru_r \rangle_{t,r \leq R_{\rm TC},\theta} = 0.408K\Lambda[\langle ru_\theta \rangle_{t,r \leq R_{\rm TC},\theta}]_{z^{\rm bot}}^{z^{\rm top}}$ (fitted with confidence interval 0.95), as predicted by the MTPC scaling for the mean flow (15). The concentration around the origin $(u_r \simeq 0)$ of all points at $\Lambda = 0$ confirms that the flow across the TC is controlled by the classical TPC in the absence of magnetic field, so that averages within the TC provide

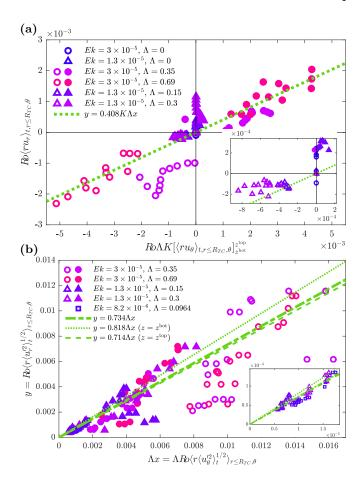


FIG. 3. Radial vs. azimuthal velocities, azimuthally and radially averaged within the TC (a) time-averaged velocities (b) rms of velocity fluctuations, and fit to corresponding scaling relations derived from the MTPC. Full (open) symbols: measurements at $z=z^{\rm bot}$ ($z=z^{\rm top}$). Different markers of the same type correspond to different thermal forcing, spanning $5\times 10^{-4} \le Ro \le 0.3$ across all cases.

a good measure of the flow across it. Radial averaging still incurs some data scattering, as flows recirculating within the TC (e.g through convective plumes) add a contribution to $\langle ru_r \rangle_{t,r \leq R_{TC},\theta}$ that is not constrained by the MTPC. A measure of this effect is captured by the nonzero values of $\langle ru_r \rangle_{t,r \leq R_{TC},\theta}$ for $\Lambda=0$ visible in the inset: it introduces a greater relative error where either the velocities or Λ are small. Nevertheless, the linear trend imposed by the MTPC clearly dominates.

Lastly, the fact that LEE operates in the QSMHD regime offers additional insight into the MTPC: since $\partial_t A \sim Rm|\mathbf{u} \times \hat{\mathbf{e}}_z|$, it can be neglected in Eq. (4) so that Eq. (14) applies at each time t, instead of only on average. Hence, in QSMHD regimes, the MTPC applies to velocity fluctuations \mathbf{u}' too. Azimuthal averages of rms of velocity fluctuations are, unlike the time-averaged velocities, not constrained by global mass conservation, so the gradients of u'_r and u'_θ share similar length scales: data from both planes collapse on almost the same fitted line $\langle ru'_r^2 \rangle_{t,r \leq R_{\mathrm{TC}},\theta}^{1/2} = 0.734 \Lambda \langle ru'_\theta^2 \rangle_{t,r \leq R_{\mathrm{TC}},\theta}^{1/2}$, shown in Fig. 3

(b), with similar slopes for top and bottom planes. This shows not only that the average flow through the TC is controlled by the MTPC, but that so are its fluctuations within the QSMHD regime.

These results show that when magnetic field and background rotation are aligned, the MTPC reshapes the global structure of flows near geostrophic contours such as planetary TCs. The MTPC provides a quantitative tool to predict the topology of such flows dominated by competing Coriolis and Lorentz forces. Indeed, the evidence in LEE that a polar magnetic field incurs a meridional flow in the polar region, but also significantly enhances the zonal flow there provides quantitative theoretical support to recent dynamo simulations and observations where these phenomena occur [7, 20, 24]. The MTPC also offers a theoretical framework to extend the current understanding of how the TPC shapes convective Taylor columns in rotating convection [11, 45] to similar structures observed in magnetorotating convection [10, 19, 46]. In actual planetary interiors, however, the MTPC only applies in regions of axial magnetic field (Eqs. (5), (6)) and so may need amending to capture the topology of meridional TC flows incorporating the magnetic field topology [47]. Similarly, with the generalized MTPC (11) incorporating conducting, permeable

and moving boundaries, more complex dynamics at the solid-liquid core boundary, such as unsteadiness due to the solidification-remelting cycle of the inner core [48], or stratification [49] may also be accounted for. Finally, the MTPC applies to magnetorotating flows in general, so its implications beyond geophysics and astrophysics also concern numerous other fields such as material science, e.g. alloy casting and stirring or crystal growth [50].

ACKNOWLEDGMENTS

The authors are grateful to the European Magnetic Field Laboratory (EMFL) and the Laboratoire des Champs Magnétiques Intense-Grenoble (CNRS) for support and access to unique magnets with high magnetic field in sufficiently large bores to conduct fluid mechanics experiments. Subscription to EMFL is funded by EP-SRC grant no. NS/A000060/1. This work was supported by Leverhulme Trust grants no. RPG-2012-456 and no. RPG-2017-366, and EPSRC grant no. EP/X010937/1. No Artificial Intelligence technology was used in this work, besides spell-checking.

- [1] J. Proudman, On the motion of solids in a liquid possessing vorticity, Proc. R. Soc. A **92**, 408 (1916).
- [2] G. I. Taylor, Motion of solids in fluids when the flow is not irrotational, Proc. R. Soc. A 93, 99 (1917).
- [3] H. P. Greenspan, *Theory of Rotating Fluids, The* (Cambridge University Press, Cambridge, England, 1969).
- [4] F. Takahashi, M. Matsushima, and Y. Honkura, Dynamo action and its temporal variation inside the tangent cylinder in MHD dynamo simulations, Phys. Earth Planet. Inter. 140, 53 (2003).
- [5] C. A. Jones and B. Sreenivasan, Azimuthal winds, convection and dynamo action in the polar regions of planetary cores, Geophys. Astrophys. Fluid Dyn. 100, 319 (2006).
- [6] F. Garcia, J. Sánchez, and M. Net, Antisymmetric Polar Modes of Thermal Convection in Rotating Spherical Fluid Shells at High Taylor Numbers, Phys. Rev. Lett. 101, 194501 (2008).
- [7] N. Schaeffer, D. Jault, H.-C. Nataf, and A. Fournier, Turbulent geodynamo simulations: a leap towards Earth's core, Geophys. J. Int. **211**, 1–29 (2017).
- [8] T. Gastine and J. M. Aurnou, Latitudinal regionalization of rotating spherical shell convection, J. Fluid Mech. 954, R1 (2023).
- [9] E. Dormy, Strong-field spherical dynamos, J. Fluid Mech. 789, 500 (2016).
- [10] S. Horn and J. M. Aurnou, The Elbert range of magnetostrophic convection. I. linear theory, Proc. R. Soc. A., 20220313 (2022).
- [11] I. Grooms, K. Julien, J. B. Weiss, and E. Knobloch, Model of Convective Taylor Columns in Rotating Rayleigh-Bénard Convection, Phys. Rev. Lett. 104,

- 224501 (2010).
- [12] R. P. J. Kunnen, The geostrophic regime of rapidly rotating turbulent convection, J. Turbul. 22, 267 (2021).
- [13] R. E. Ecke and O. Shishkina, Turbulent rotating Rayleigh-Bénard convection, Annu. Rev. Fluid Mech. 55, 603 (2023).
- [14] Chandrasekhar, Hydrodynamic and Hydromagnetic Stability (Clarendon, Oxford, 1961).
- [15] I. A. Eltayeb, Hydromagnetic convection in a rapidly rotating fluid layer, Proc. R. Soc. A 326, 229 (1972).
- [16] I. A. Eltayeb, Overstable hydromagnetic convection in a rotating fluid layer, J. Fluid Mech. 71, 161 (1975).
- [17] P. H. Roberts and E. M. King, On the genesis of the Earth's magnetism, Rep. Prog. Phys. 76, 096801 (2013).
- [18] K. Aujogue, A. Pothérat, and B. Sreenivasan, Onset of plane layer magnetoconvection at low Ekman number, Phys. Fluids 27, 106602 (2015).
- [19] S. Horn and J. Aurnou, The Elbert range of rotating magnetoconvection II: comparison between linear theory to nonlinear low-Rm simulations, Proc. R. Soc. A (to be published).
- [20] H. Cao, R. K. Yadav, and J. M. Aurnou, Geomagnetic polar minima do not arise from steady meridional circulation, Proc. Natl. Acad. Ssi. U.S.A. 115, 11186 (2018).
- [21] H. Hotta, Breaking Taylor-Proudman balance by magnetic fields in stellar convection zones, Astrophys. J. Lett. 860, L24 (2018).
- [22] A. Sakuraba, Linear magnetoconvection in rotating fluid spheres permeated by a uniform axial magnetic field, Geophys. Astrophys. Fluid Dyn. 96, 291 (2002).
- [23] S. J. Mason, C. Guervilly, and G. R. Sarson, Magnetoconvection in a rotating spherical shell in the presence

- of a uniform axial magnetic field, Geophys. Astrophys. Fluid Dyn. **116**, 458 (2022).
- [24] C. Finlay, N. Gillet, J. Aubert, P. Livermore, and D. Jault, Gyres, jets and waves in the earth's core., Nat. Rev. Earth Environ. 4, 377 (2023).
- [25] J. Sommeria and R. Moreau, Why, how and when MHD turbulence becomes two-dimensional, J. Fluid Mech. 118, 507 (1982).
- [26] Y. B. Kolesnikov and A. B. Tsinober, Experimental investigation of two-dimensional turbulence behind a grid, Fluid Dyn. 9, 621 (1974).
- [27] R. Klein and A. Pothérat, Appearance of Three-Dimensionality in Wall-Bounded MHD Flows, Phys. Rev. Lett. 104, 034502 (2010).
- [28] N. T. Baker, A. Pothérat, L. Davoust, and F. Debray, Inverse and Direct Energy Cascades in Three-Dimensional Magnetohydrodynamic Turbulence at Low Magnetic Reynolds Number, Phys. Rev. Lett. 120, 224502 (2018).
- [29] J. C. R. Hunt and G. S. S. Ludford, Three-dimensional MHD duct flow with strong transverse magnetic fields part 1: Obstacles in a constant area channel, J. Fluid Mech. 33, 693 (1968).
- [30] Kulikovskii, Flows of a conducting incompressible liquid in an arbitrary region with a strong magnetic field, Fluid Dyn. 8, 462 (1973).
- [31] T. Alboussière, J. P. Garandet, and R. Moreau, Asymptotic analysis and symmetry in MHD convection, Phys. Fluids 8, 2215 (1996).
- [32] J. M. Aurnou, S. Horn, and K. Julien, Connections between nonrotating, slowly rotating, and rapidly rotating turbulent convection transport scalings, Phys. Rev. Res. 2, 043115 (2020).
- [33] G. Schubert and K. Soderlund, Planetary magnetic fields: Observations and models, Phys. Earth Planet. Inter. 187, 92 (2011).
- [34] D. J. Acheson, Hydromagnetics in rotating fluids, Rep. Prog. Phys. 36, 159 (1973).
- [35] K. Aujogue, A. Pothérat, I. Bates, F. Debray, and B. Sreenivasan, Little Earth Experiment: an instrument to model planetary cores, Rev. Sci. Instrum. 87, 084502 (2016).
- [36] K. Aujogue, A. Pothérat, B. Sreenivasan, and F. Debray, Experimental study of the convection in a rotating tangent cylinder, J. Fluid Mech. 843, 355 (2018).
- [37] K. Aujogue, The Little Earth Experiment: a journey towards the Earth tangent cylinder, Ph.D. thesis, Coventry University (2016).
- [38] O. Andreev, Y. Kolesnikov, and A. Thess, Visualization of the Ludford column, J. Fluid Mech. 721, 438 (2013).
- [39] B. Moudjed, A. Pothérat, and M. Holdsworth, PIV measurements of pressure and velocity fields in the plane magnetohydrodynamic Couette flow, Exp. Fluids 61, 255 (2020).
- [40] A. M. Grannan, J. S. Cheng, A. Aggarwal, E. K. Hawkins, Y. Xu, S. Horn, J. Sánchez-Álvarez, and J. M. Aurnou, Experimental pub crawl from Rayleigh-Bénard to magnetostrophic convection, J. Fluid Mech. 939, R1 (2022).
- [41] T. Vogt, J.-C. Yang, F. Schindler, and S. Eckert, Free-fall velocities and heat transport enhancement in liquid metal magneto-convection, J. Fluid Mech. 915, A68 (2021).
- [42] P. H. Roberts, Introduction to Magnetohydrodynamics

- (Longmans, New York, 1967).
- [43] J. Aurnou, S. Andreadis, L. Zhu, and P. Olson, Experiments on convection in Earth's core tangent cylinder, Earth Plan. Sci. Lett. 212, 119 (2003).
- [44] See Supplemental Material for the method to calculate K(z) in Eq. (15) from experimental data.
- [45] D. Nieves, A. M. Rubio, and K. Julien, Statistical classification of flow morphology in rapidly rotating Rayleigh-Bénard convection, Phys. Fluids 26, 086602 (2014).
- [46] M. Yan, M. A. Calkins, S. Maffei, K. Julien, S. M. Tobias, and P. Marti, Heat transfer and flow regimes in quasistatic magnetoconvection with a vertical magnetic field, J. Fluid Mech. 877, 1186 (2019).
- [47] Nonaxial fields could be incorporated in the MTPC following the steps leading to Eq. (14), as long as the axial Lorentz force is at most $\mathcal{O}(Ro)$.
- [48] T. Alboussière, R. Deguen, and M. Melzani, Meltinginduced stratification above the Earth's inner core due to convective translation, Nature (London) 466, 744 (2010).
- [49] M. de la Torre Juárez, Taylor-Proudman columns in nonhydrostatic divergent baroclinic and barotropic flows, Q. J. R. Meteorol. Soc 135, 2179 (2009).
- [50] I. Grants, J. Pal, and G. Gerbeth, Physical modelling of Czochralski crystal growth in horizontal magnetic field, J. of Cryst. Growth 470, 58 (2017).

Method to calculate K(z) in Eq. (15) from experimental data

We now simplify the general expression of the MTPC in Eq. (14) for the purpose of comparing its prediction to the data obtained from LEE. To this end, since the TC is axisymmetric, and more generally in planetary context, geostrophic contours are circular, the directions tangential and normal to them s and n are respectively the azimuthal and cylindrical-radial coordinates (bearing in mind that geostrophic contours are defined in the z-averaged plane). Further averaging (14) along the azimuthal direction yields a simpler equation linking radial and azimuthal velocity components:

$$\Delta_{rz} \langle B_z^{-1} (u_r - u_0) \rangle_{t,\theta} + \Lambda \partial_{zz}^2 \langle B_z u_\theta \rangle_{t,\theta} = 0.$$
 (1)

Additionally, in the case of LEE, the magnetic field is assumed homogeneous ($B_z = 1$) and the top and bottom boundaries impermeable and electrically insulating ($u_0 = 0$). To obtain more reliable estimates from the measurements and reduce the noise associated to the measurement over the single line following the TC boundary, we average (1) over horizontal sections of the TC (Distances are henceforth normalised by the TC's radius $R_{\rm TC}$ for simplicity):

$$\partial_r \langle u_r \rangle_{t,\theta,r=1} + \partial_{zz}^2 \langle r u_r \rangle_{t,\theta,r<1} + \Lambda \partial_{zz}^2 \langle r u_\theta \rangle_{t,\theta,r<1} = 0.$$
 (2)

Up to this point, the MTPC is still in exact form. We now need to estimate its different terms using data available to us from PIV measurements. The radial velocity at the TC boundary is estimated from its average over the TC's horizontal cross section i.e. at constant z, again to reduce noise:

$$\langle u_r \rangle_{t,\theta,r=1} \simeq \langle r u_r \rangle_{t,\theta,r<1}.$$
 (3)

Then, taking the TC radius as lengthscale for the radial derivative, the first term in Eq. (1) is estimated at each of the PIV measurement planes as:

$$\partial_r \langle u_r(z=z^{\text{bot}}) \rangle_{t,\theta,r=1} \simeq \epsilon_r^{\text{bot}} \langle r u_r \rangle_{t,\theta,r<1}$$
 (4)

$$\partial_r \langle u_r(z=z^{\text{top}}) \rangle_{t,\theta,r=1} \simeq \epsilon_r^{\text{top}} \langle r u_r \rangle_{t,\theta,r<1}$$
 (5)

Here, $\epsilon_r^{\rm bot}$ and $\epsilon_r^{\rm top}$ are either 1 or -1 to reflect the concavity of the radial velocity profiles (see figure 2a in the main text) that implies that where the radial velocity is mostly positive (resp. negative) within the TC, its radial derivative at the TC boundary is negative (resp. positive). The horizontal PIV does not provide us with access to the vertical derivatives so they must be estimated from the measurements in the top and bottom planes, respectively at $z=z^{\rm bot}$ and $z=z^{\rm top}$. Using the distance between the two PIV planes $\Delta h_{\rm PIV}$ as lengthscale for the vertical derivatives of azimuthal velocity yields an estimate for the second derivative applicable to both planes:

$$\partial_{zz} \langle r u_{\theta} \rangle_{t,\theta,r \leq 1} \simeq [\langle r u_{\theta}(z^{\text{top}}) \rangle_{t,\theta,r \leq 1} - \langle r u_{\theta}(z^{\text{bot}}) \rangle_{t,\theta,r \leq 1}] / \Delta h_{\text{PIV}}^{2},$$

$$\simeq [\Lambda \langle r u_{\theta} \rangle_{t,\theta,r \leq 1}]_{z=z^{\text{top}}}^{z=z^{\text{top}}} / \Delta h_{\text{PIV}}^{2}.$$
(6)

Unlike the azimuthal velocity, the azimuthal and time-averaged radial velocity, is constrained by mass conservation imposing that its sum over the TC surface must be zero. To take advantage of this property, we assume, based on the profiles of radial velocity in figure 2(a)), that the meridional recirculation consists of a single cell, represented on figure 1: The radial flow $\sim u_r^{\rm top}$ enters (or exits) the upper part of the TC over a height $\sim l_z^{\rm top}$ and $\sim u_r^{\rm bot}$ and exits (or enters) it in the bottom part over a height $l_z^{\rm bot} = h_{\rm TC} - l_z^{\rm top}$. Mass conservation then imposes that

$$u_r^{\text{top}} l_z^{\text{top}} \simeq -u_r^{\text{bot}} l_z^{\text{bot}}.$$
 (7)

Top and bottom radial velocities through the upper and lower sections are estimated using the PIV measurements in the top and bottom planes averaged over horizontal cross-sections of the TC, $u_r^{\text{top}} \simeq \langle ru_r(z=z^{\text{top}}) \rangle_{t,\theta,r\leq 1}$ and $u_r^{\text{bot}} \simeq \langle ru_r(z=z^{\text{bot}}) \rangle_{t,\theta,r\leq 1}$. $l_z^{\text{top/bot}}$ are then obtained by solving the mass conservation (7) together with the constraint that $l_z^{\text{top}} + l_z^{\text{bot}} = h_{\text{TC}}$.

$$l_z^{\text{bot}} = \frac{u_r^{\text{top}}}{u_r^{\text{top}} - u_r^{\text{bot}}} h_{\text{TC}},\tag{8}$$

$$l_z^{\text{top}} = -\frac{u_r^{\text{bot}}}{u_r^{\text{top}} - u_r^{\text{bot}}} h_{\text{TC}}.$$
 (9)

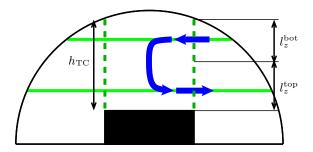


FIG. 1. Schematic meridional section of LEE representing the heater (in black), the TC (green dashed line) and the one-cell meridional recirculation assumption (flow direction in blue).

Then using l_z^{top} and l_z^{bot} as lengthscales for the vertical derivatives of radial velocities in the the in- and outflow regions of the TC respectively provides us with the estimates:

$$\partial_{zz}^2 \langle ru_r \rangle (z = z^{\text{bot}}) \simeq \epsilon^{\text{bot}} \langle ru_r (z = z^{\text{bot}}) \rangle_{t,\theta,r \le 1} / (l_z^{\text{bot}})^2,$$
 (10)

$$\partial_{zz}^{2} \langle ru_{r} \rangle (z = z^{\text{top}}) \simeq \epsilon^{\text{top}} \langle ru_{r}(z = z^{\text{top}}) \rangle_{t,\theta,r \le 1} / (l_{z}^{\text{top}})^{2}. \tag{11}$$

Here $\epsilon^{\rm bot}$ and $\epsilon^{\rm top}$ take the values 1 or -1 to reflect the local concavity of the z-profile of radial velocity imposed by the signs of $\langle ru_r(z=z^{\text{bot}})\rangle_{t,\theta,r\leq 1}$ and $\langle ru_r(z=z^{\text{top}})\rangle_{t,\theta,r\leq 1}$ to form a single-cell meridional recirculation. Gathering all estimates, (1) eventually leads to the scaling relation (15) from the main text:

$$\langle ru_r(z)\rangle_{t,\theta,r\leq 1} \sim K(z)\Lambda[\langle ru_\theta\rangle_{t,\theta,r\leq 1}]_{z^{\text{bot}}}^{z^{\text{top}}},$$
(12)

where the coefficient K(z) is calculated in each PIV measurement plane as:

$$K(z=z^{\text{bot}}) = -\frac{(l_z^{\text{bot}})^2}{\Delta h_{\text{PIV}}^2 \left[\epsilon_r^{\text{bot}} (l_z^{\text{bot}})^2 + \epsilon^{\text{bot}}\right]},\tag{13}$$

$$K(z = z^{\text{bot}}) = -\frac{(l_z^{\text{bot}})^2}{\Delta h_{\text{PIV}}^2 \left[\epsilon_z^{\text{bot}} (l_z^{\text{bot}})^2 + \epsilon^{\text{bot}} \right]},$$

$$K(z = z^{\text{top}}) = -\frac{(l_z^{\text{top}})^2}{\Delta h_{\text{PIV}}^2 \left[\epsilon_r^{\text{top}} (l_z^{\text{top}})^2 + \epsilon^{\text{top}} \right]}.$$
(13)

In practice, measurements in both PIV planes at $z=z^{\rm bot}$ and $z=z^{\rm top}$ are required to estimate the r.h.s. of Eq. (12) at each of the two PIV measurement planes. Hence, each set of PIV measurements in both planes for a given set of parameters Ek, Λ , Ro returns two points in figure 3a, one for each plane (denoted by open and full symbols).